RESEARCH

High-performance eco-friendly tamarind gum-based biopolymer electrolytes for electric double-layer capacitor application

P. Saranya[1,2] · K. Sundaramahalingam[2] · D. Vanitha[3] · M. Nandhinilakshmi[1,2] · V. N. Vijayakumar[4]

Abstract

Mg^+-ion-conducting tamarind gum (TG)-based biopolymer electrolytes (BPEs) are prepared by a simple solution-casting technique. XRD and FTIR analyses have revealed the dissociation and complexation of the salt with the polymer host. The glass transition temperature is observed for all the prepared electrolytes using differential scanning calorimetry (DSC). By using AC impedance analysis, the higher ionic conductivity calculated for the sample 1-g TG with 0.5 g of salt (5 TML) is 3.48×10^{-3} S/cm. The temperature-dependent conduction mechanism of sample 5 TML follows three models: region I obeys the overlapping-large polaron tunneling (OLPT) model, the quantum mechanical tunneling (QMT) model is observed in region II, and region III obeys the nonoverlapping small polaron tunneling (NSPT) model. The minimum activation energy of 0.045 eV is observed for sample 5 TML according to the Arrhenius plot. The complex dielectric permittivity and dielectric modulus spectra are discussed. The relaxation time (τ) attained by tangent analysis for 5 TML is 7.94×10^{-7} s. From the transference number measurement, it is concluded that the conductivity is mostly due to the transfer of ions only. Using the 5 TML sample, a symmetrical supercapacitor and an electrochemical cell are fabricated. Cyclic voltammetry (CV) reveals a specific capacitance of 413.05 Fg^{-1} at a low scan rate of 15 mV/s. From the GCD data, the power and energy density are calculated as 1499 W/kg and 100 Wh/kg, respectively. The cyclic stability is confirmed by the observed constant values of power and energy densities for different cycles.

Keywords Conduction mechanism · CV · GCD · DSC · AC impedance · Supercapacitor

Introduction

The massive use of coal and petroleum is an inevitable part of modern lifestyles for energy consumption and has resulted in significant environmental pollution. There are many alternative renewable resources used instead of fossil fuels. The power needs of the world can be satisfied by renewable energy sources, such as wind turbines, hydroelectric dams, solar panels, and geothermal energy. Storage of the energy harvested from renewable sources is consequently necessary for its later usage since renewable sources are not spontaneous sources of energy. In addition, the development of energy storage electronic devices is needed for effective energy storage [1, 2]. Electrolytes are the key component of energy storage devices such as batteries and supercapacitors and are currently attracting an abundance of research attention. Their primary function is to conduct ions between the electrodes, enabling the electrochemical reactions that generate or store energy. The performance, safety, and longevity of these devices are heavily influenced by the properties of the electrolytes used. Electrolytes can be broadly classified into three main types: *liquid electrolytes*, *solid electrolytes*, and *gel electrolytes*. Many liquid electrolytes are highly flammable. Liquid electrolytes can leak from the device if the casing is compromised, leading to potential

✉ D. Vanitha
vanibala2003@gmail.com

1 Multifunctional Materials Laboratory, International Research Centre, Kalasalingam Academy of Research and Education, Srivilliputhur, Tamil Nadu, Krishnankoil, 626 126, India

2 Department of Science and Humanities, P.S.R.R College of Engineering, Sivakasi 626 140, Tamil Nadu, India

3 Department of Physics, Kalasalingam Academy of Research and Education, Krishnankoil, Srivilliputhur, Tamil Nadu 626 126, India

4 Condensed Matter Research Laboratory, Department of Physics, Bannari Amman Institute of Technology, Sathyamangalam, Tamil Nadu 638401, India

damage to the device and creating safety hazards. Gel electrolytes typically have lower ionic conductivity than liquid electrolytes. Solid electrolytes are non-flammable and can potentially enable the use of high-voltage electrodes and metallic lithium anodes, increasing energy density.

For the preparation of solid electrolytes, polymers can be used. Polymers are macromolecules because they consist of a large number of monomer units. Polymers can be divided into two types. One is a synthetic polymer, and the other is a biopolymer. Synthetic polymers are nondegradable and increase environmental problems [3]. For example, the synthetic polymer PVP has an ionic conductivity on the order of 10^{-11} S/cm [4]. Recently, the use of bio-based materials which are derived from renewable resources has increased because the world is currently experiencing a serious crisis related to sustainability and environmental issues [5]. Many studies have been performed with natural polymers such as agar−agar [6–8], chitosan [9], dextran [10], methylcellulose [11–13], starch [14], pectin [15], carrageenan [16–19], and gum-based polymers [20, 21].

Tamarind gum (TG) or tamarind seed polysaccharide is obtained from the seeds of *Tamarindus indica* [22]. TG functions as a highly branched carbohydrate composed of glucose, xylose, and galactose units that exists in a ratio of 2.8:2.25:1.0 along with side chains of xylopyranose and (1,6)-linked [-D-galactopyranosyl-(1,2)-D-xylopyranosyl] to glucose residues [23]. TG is a renewable and earth-abundant polysaccharide that is highly soluble in hot water and used in many industrial applications [24]. Specifically, the properties of solid polymer electrolytes (SPEs) are better than those of liquid or gel polymer electrolytes [25]. SPEs have many remarkable properties including low volatility, leak-proof construction, lack of solvents, and good thermal, electrical, mechanical, volumetric, and electrochemical stabilities. Due to their diverse and beneficial characteristics, SPEs have achieved remarkable success in electronic industrial applications [26, 27].

The conductivity of a polymer electrolyte can be improved by adding salts, plasticizers, nanofillers, and ionic liquids. The majority of research is focused on monovalent salt systems (H^+, Li^+, and Na^+) [4, 28–33]. Magnesium is the eighth most abundant element in the Earth's crust, making it significantly more available than lithium. Magnesium seems to be the most promising material among the other due to its potential for greater volumetric-specific capacity. Unlike lithium and sodium, which are monovalent, magnesium is divalent. This means that each Mg^{2+} ion can transfer two electrons per ion, potentially offering a higher-energy density. This can lead to a higher theoretical capacity compared to lithium-ion and sodium-ion batteries. The higher charge density of Mg^{2+} ions allows for more compact energy storage, potentially leading to batteries with higher-energy densities.

Magnesium salts generally have lower environmental toxicity compared to lithium salts. Magnesium chloride is an inorganic salt that dissolves easily in water. In food preparation, pharmaceuticals, agriculture, marine applications, bath salts, and flotation tanks, magnesium chloride can be used [34].

In this work, magnesium salt is chosen to enhance the conductivity of the TG. M. Sundar et al. have reported that poly(ethylene oxide) (PEO) and magnesium chloride doped with filler B_2O_3 have attained a maximum conductivity of 4.52×10^{-6} S/cm at room temperature [35]. The triblock copolymer poly(vinylidene chloride-co-acrylonitrile-co-methyl methacrylate) (poly(VdCl-co-AN-co-MMA)) with magnesium chloride has a maximum conductivity of 1.89×10^{-5} S/cm at ambient temperature [36]. Several methods have been developed for producing cost-effective energy storage devices, but there is a problem in making batteries with good performance. To address these issues, SPEs can be developed using an affordable solution-casting process with increased ionic conductivity. It has improved electrochemical and physical characteristics to be used in energy storage devices such as supercapacitors and solid-state batteries.

Materials

Tamarind seed polysaccharide (TSP) was obtained from Tokyo Chemical Industry, Japan. The magnesium ion source magnesium chloride hexahydrate ($MgCl_2 \cdot 6H_2O$) salt with a molecular weight of 203.31 g/mol was obtained from Chemspure, Chennai. Double distilled water was used as the solvent. For electrode preparation, activated carbon, poly(vinylidene fluoride) (PVdF), and N-methyl pyrrolidone (NMP) were procured from Sanwa Components, Inc.

Preparation method

All the polymer electrolytes were prepared by the simple solution-casting technique. In this work, 1 g of TSP was dissolved in 50 ml of double distilled water at 80 °C for 5 h of vigorous stirring with a magnetic stirrer at 1500 rpm. Different concentrations of salt were dissolved in 20 ml of double distilled water, and the notations are given in Table 1. After dissolving the salt, TSP was added dropwise. The blended solution was stirred for 24 h. The homogeneous solutions were poured into Petri dishes and maintained at 60 °C in an oven for 24 h. Then, the transparent thin films are peeled off from the Petri dishes with a thickness of 0.022 cm, as shown in Fig. 1a.

Table 1 Polymer-salt composition and its sample codes

Polymer and salt concentration	Sample code
Pure tamarind gum	TSP
1 g of TSP + 0.1 g of $MgCl_2$	1 TML
1 g of TSP + 0.2 g of $MgCl_2$	2 TML
1 g of TSP + 0.3 g of $MgCl_2$	3 TML
1 g of TSP + 0.4 g of $MgCl_2$	4 TML
1 g of TSP + 0.5 g of $MgCl_2$	5 TML
1 g of TSP + 0.6 g of $MgCl_2$	6 TML

Fabrication of the symmetrical supercapacitor

N-methyl pyrrolidone (NMP), poly(vinylidene fluoride) (PVdF), and activated carbon were used at a ratio of 8:1:1 for electrode preparation. Using a mortar and pestle, PVdF, activated carbon, and NMP were mixed to form the slurry. Then, it was coated in a nickel foil. To stop the formation of moisture, the sample was dried for 12 h at 80 °C. The arrangement of the electrode and electrolyte in the symmetrical supercapacitor device is shown in Fig. 1b.

Results and discussion

XRD analysis

Figure 2a displays the typical XRD patterns of TSP and different weight percentages of magnesium chloride-doped TSP polymer electrolytes. TSP shows a broad diffraction halo at $2\theta = 19.6°$, $30.1°$, and $41.1°$ [37]. With the addition of salt, the intensity of the small humps at $2\theta = 19.6°$ is decreased. There is a slight increase in the hump at $2\theta = 30.1°$ and $41.1°$ due to the addition of salt. For the sample 5 TML, the intensity of all the humps decreases, and the sample is highly amorphous [38, 39]. No crystalline peaks of magnesium

chloride are observed which indicates the complete dissolution of salt with the polymer, and the JCPDS of pure magnesium chloride ($2\theta = 15.4°$, $36.4°$, and $50°$ (JCPDS-89–1567)) is shown in Fig. 2a.

The degree of crystallinity χ can be determined by the deconvolution of the XRD peaks. In the XRD pattern, the high-intensity peak at $2\theta = 19.6°$ is considered as the crystalline peak. The formula for calculating the degree of crystallinity (χ (%)) is given below:

$$\chi(\%) = A_C/A_T \times 100 \tag{1}$$

Here, A_C is the area of crystallinity, and A_T represents the total area of the peak. By deconvoluting the XRD peaks, the degree of crystallinity is decreased with increasing salt concentration. The values are given in Table 2. The intensity of the hump at $2\theta = 30.1°$ is slightly increased for sample 6 TML.

FTIR spectrum analysis

The possible interactions between TSP and salt are shown in Fig. 3a. FTIR spectroscopy is a unique tool for investigating the complex nature of polymers and salts. The FTIR spectra of all the synthesized samples are shown in Fig. 3b. The band assignments for the peak values are given in Table 3.

The vibrational spectra of TSP show bands at 3373 cm^{-1}, 2900 cm^{-1}, 1645 cm^{-1}, 1362 cm^{-1}, 1018 cm^{-1}, 938 cm^{-1}, and 890 cm^{-1}. The peak attributed to the hydroxyl group (O–H) stretching of the glucan backbone of TSP at 3373 cm^{-1} is shifted slightly due to the addition of salt [40]. In TSP, the transmittance peak at 2900 cm^{-1} corresponds to CH_2 asymmetric stretching and shifts to 2928 cm^{-1} [24]. The transmittance peak at 1651 cm^{-1} is attributed to C=C stretching, and the intensity of that particular transmittance peak increases with increasing salt ratio [41]. This indicates

Fig. 1 **a** Prepared solid polymer electrolyte. **b** Schematic representation of symmetrical supercapacitor

Prepared Solid Polymer Electrolyte

a

Mg ion conducting Polymer electrolyte

Cathode

Anode
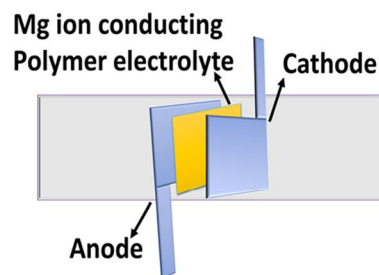
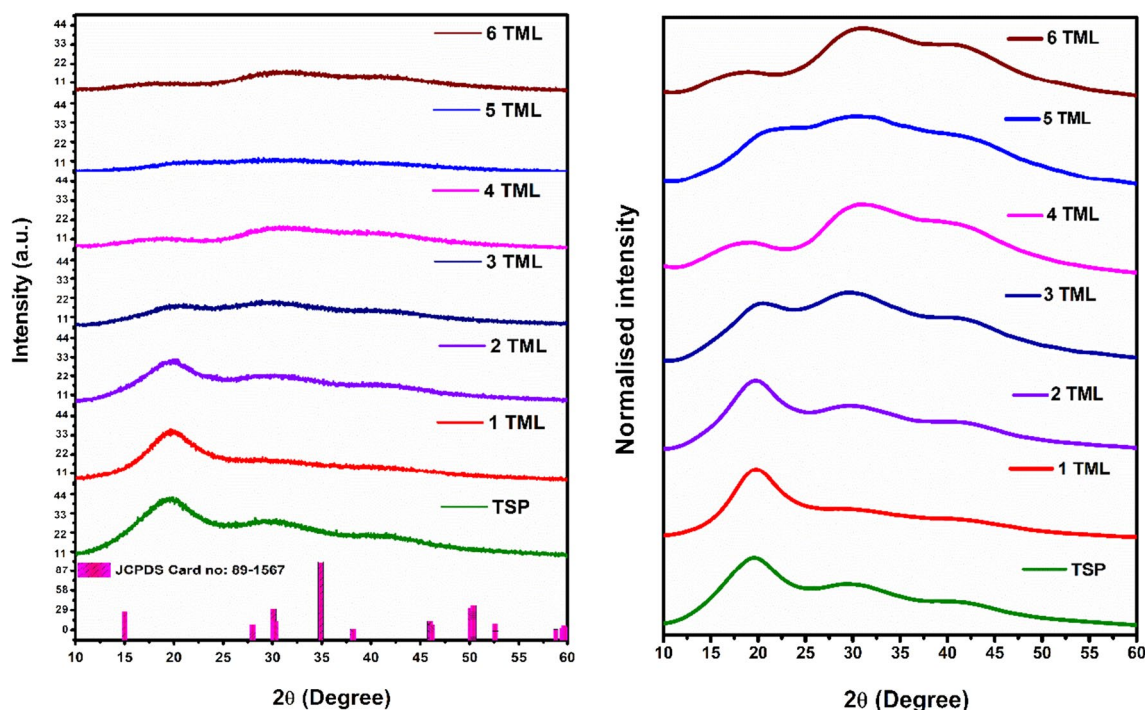**Fabrication of Symmetrical supercapacitor**

b

Fig. 2 XRD pattern of polymer electrolytes

Table 2 Degree of crystallinity of polymer electrolytes

Polymer electrolytes	Degree of crystallinity (%)
TSP	41.3
1 TML	37.2
2 TML	25.0
3 TML	21.5
4 TML	18.0
5 TML	**10.6**
6 TML	12.6

the incorporation of magnesium chloride with TSP. The band at 1362 cm^{-1} is attributed to CH$_2$ plane bending [37]. A strong C–O stretching vibration is observed at 1020 cm^{-1}. With increasing the salt ratio, the intensity of this transmittance peak decreases. The transmittance peak intensity decreases with increasing salt ratio in the range of 938 to 890 cm^{-1} which is due to C–H out-of-plane bending and C-anomeric group stretching of the polysaccharide respectively [42].

DSC analysis of polymer electrolytes

Differential scanning calorimetry is employed to determine the glass transition temperature (T_g) of the prepared biopolymer electrolytes. Approximately, 3.4 mg of biopolymer

electrolyte is placed in an aluminum pan under a nitrogen gas atmosphere and hermetically sealed. The glass transition temperature of the polymer is the temperature at which the polymer electrolyte changes its behavior from the flexible state to the glassy state [43].

A DSC plot of all the prepared electrolytes is shown in Fig. 4. The TSP sample has a T_g value of 59 °C. The addition of magnesium salt with TSP increases the T_g. For the higher conducting sample 5 TML, the glass transition temperature is 127 °C which is due to two main factors: (1) elongation of the polymer chain because of electrostatic repulsion in the polymer chain and (2) changes in the density of the solid polymer electrolyte [44]. This phenomenon has been explained as the result of less segmental motion resulting from an increase in the intermolecular coordination between the hydrogen and the oxygen atom in the polymer chain [45]. The higher conducting sample 5 TML has large number of free charge carriers which is the main reason for the increase in the glass transition temperature [46]. The T_g values of all the samples are given in Table 4.

AC impedance analysis

Nyquist plot

Nyquist plots are typically produced using impedance measurements and can have three different configurations: (i) a tilted spike, (ii) a depressed semicircle, or (iii) a depressed
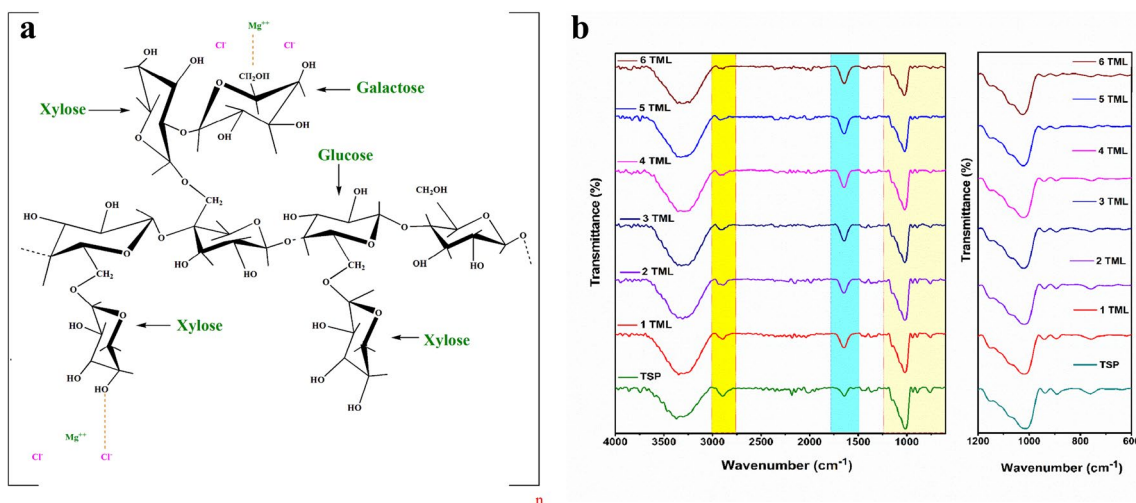
Fig. 3 **a** Chemical structure of TSP and magnesium chloride. **b** FTIR spectra of all the SPEs

Table 3 FTIR spectrum wave number and their assignments

Wave number (cm^{-1})		Assignments
TSP	MgCl$_2$-doped TSP electrolytes	
3373	3352	O–H stretching
2900	2928	CH$_2$ asymmetric stretching
1645	1651	C=C stretching
1362	1362	CH$_2$ plane bending
1018	1020	C–O stretching
938	942	C–H out-of-plane bending
890	894	C-anomeric group stretching of polysaccharide

semicircle combined with a tilted spike. Figure 5a and b shows the Nyquist plots of TSP and TSP with different concentrations of salt at room temperature. Figure 5a shows the Nyquist plot of TSP, which shows a semicircle. Figure 5b shows a low-frequency spike followed by a semicircle at high frequency for the salt-doped SPEs. Low-frequency spikes are noticed by the effect of the blocking electrodes. Due to the parallel combination of the bulk resistance and bulk capacitance, a high-frequency semicircle is observed. The bulk resistance (R_b) is determined by considering the high-frequency intercept of the semicircle and the low-frequency spike on the real axis (Z'). Using Z-view fitting software, the value of the bulk resistance is obtained. The AC ionic conductivity of the SPEs can be calculated by the following formula:

$$\sigma = \frac{t}{AR_b} (S/cm) \tag{2}$$
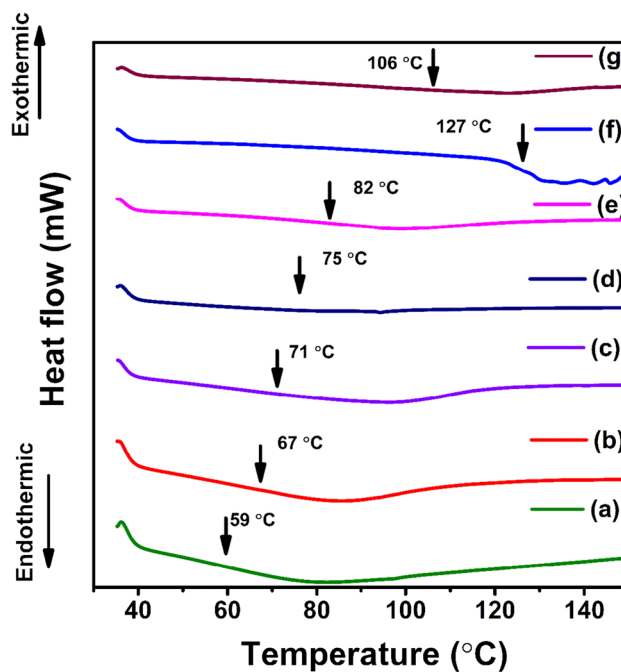
Fig. 4 Differential scanning calorimetry plots of **a** TSP, **b** 1 TML, **c** 2 TML, **d** 3 TML, **e** 4 TML, **f** 5 TML, and **g** 6 TML

Here, t is the thickness, R_b is the bulk resistance, and A represents the contact area. At ambient temperature, the ionic conductivity of the pure tamarind gum is 2.42×10^{-9} S/cm. When salt is added with TSP, the ionic conductivity of the SPEs is increased to a concentration of 0.5 g of salt with 1 g of TSP. A maximum ionic conductivity of 3.48×10^{-3} S/cm is observed at room temperature for 5 TML. The ionic conductivities of all the samples are given in Table 4. An increase in the amorphous structure of prepared electrolytes

Table 4 Calculated T_g, σ, and E_a values of SPEs

Samples	Glass transition temperature (T_g) in °C	AC conductivity (S/cm)	Activation energy (eV)
TSP	59	2.42×10^{-9}	0.30
1 TML	67	5.58×10^{-5}	0.25
2 TML	71	9.53×10^{-5}	0.21
3 TML	75	7.52×10^{-4}	0.17
4 TML	82	1.42×10^{-3}	0.09
5 TML	**127**	**3.48×10^{-3}**	**0.04**
6 TML	106	1.78×10^{-3}	0.11

reduces the energy barrier and facilitates fast ion transport along with the release of many mobile charge carriers [47]. Upon further addition of salt (0.6 g), the ionic conductivity is decreased slightly to 1.78×10^{-3} S/cm. The decrease in ionic conductivity may be due to the aggregation of ions in the polymer matrix.

Conductance spectra

The conductance spectra of the biopolymer electrolyte TSP and various concentrations of salt are displayed in Fig. 6a and b. Pure tamarind gum has two regions in its conductance spectrum. The plateau region at low frequency occurs because of the space-charge polarization between the electrode–electrolyte interface, and the high-frequency dispersion region is observed by the bulk relaxation phenomenon [21]. The conduction spectrum of the salt-added samples consists of three distinct regions.

Region I is the low-frequency dispersion region which represents the space charge polarization at the interface of the electrode and electrolyte. The frequency-independent plateau region (region II) is observed in the mid-frequency range. With the increase in salt ratio, the mid-frequency plateau region decreases. Compared with the other electrolytes, sample 5 TML has a small mid-frequency plateau region.

Due to the bulk relaxation, a high-frequency dispersion region (region III) is observed [48, 49].

Temperature-dependent conduction mechanism

Figure 6c shows the conduction mechanism of the higher conducting sample. The conduction mechanism is determined using Jonscher's universal power law by increasing the temperature from 303 to 353 K.

$$\sigma_{ac} = \sigma_{dc} + A\omega^s \tag{3}$$

$$\omega^s = \frac{\sigma_{dc}}{A} \tag{4}$$

Here, A is the temperature-dependent parameter, and ω^s is the hopping frequency. Three regions are observed in the conductance spectra. Nonlinear fitting is used for the determination of the slope (s) value. There are few models that depend on the value of the power law exponent "s," which is usually less than 1. When $T \rightarrow 0$ K, the "s" value increases towards unity, following the correlated barrier hopping (CBH) model. The temperature-independent "s" value provides information regarding the quantum mechanical tunneling model (QMT). The quantum mechanical phenomenon states that conducting ion and stress fields combine to generate the polaron. Tunneling is the mechanism by which polarons pass through a potential barrier. The increase in the "s" value due to the temperature increase is called nonoverlapping small polaron tunneling (NSPT). The overlapping-large polaron tunneling (OLPT) model is indicated by the dependence of "s" on temperature and frequency, as well as the reduction in "s" with increasing temperature [50, 51].

Region I obeys the overlapping large polaron tunneling (OLPT) model. In which, the "s_1" value decreases with increasing temperature. As a result, the lack of dependence of ions on one another facilitates tunneling rather than hopping [52]. The quantum mechanical tunneling model (QMT) is observed in region II, in which the "s2" value is constant

Fig. 5 a Nyquist plot of TSP. **b** Nyquist plot of prepared electrolytes
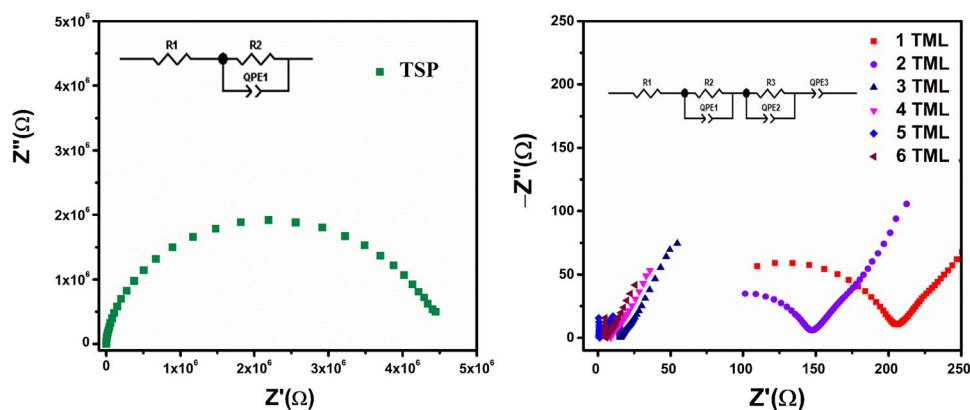
Fig. 6 **a** Conductance spectrum of TSP. **b** Conductance spectra of TSP with salt-doped SPEs. **c** Conduction mechanism for the higher conducting sample
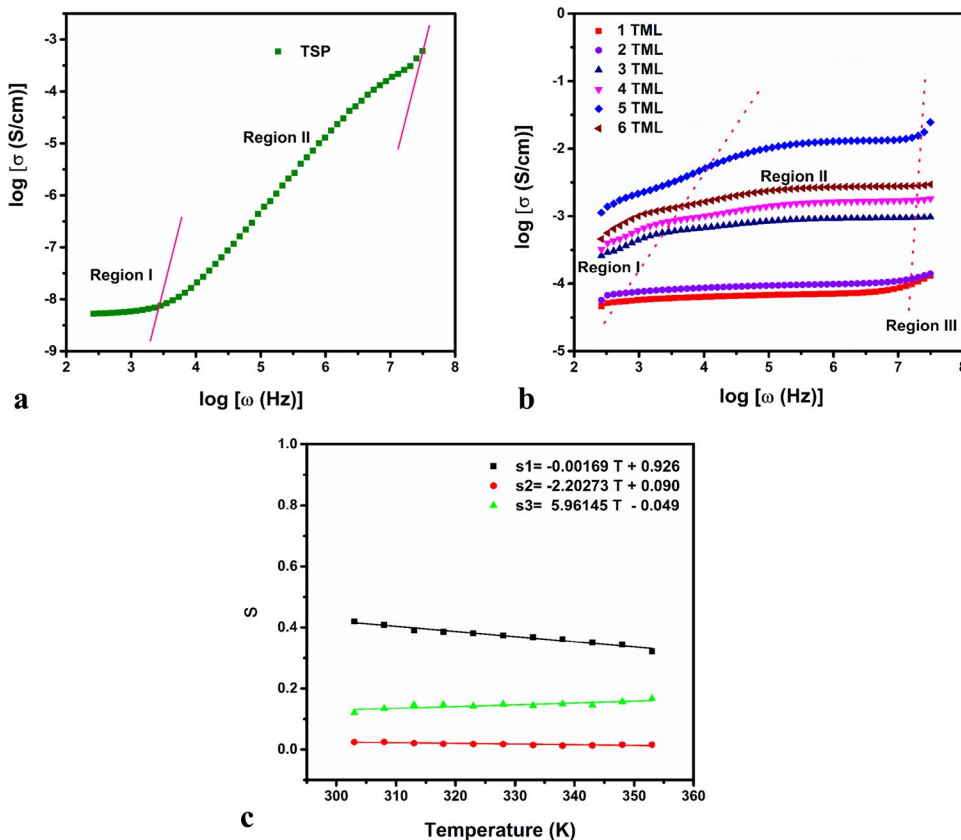
as the temperature increases. In region II, the polarons can be tunnelled through the potential barrier to nearby sites. The slope of "s3" increases with increasing temperature, which proves that the nonoverlapping small polaron tunneling (NSPT) model is applicable in region III. The equations for all the regions are shown in Fig. 6c.

Arrhenius plot

The temperature dependence of the ionic conductivity of all the prepared electrolytes from 303 to 353 K is shown

in Fig. 7a and b. The ionic conductivity of the electrolyte increases with increasing temperature. All polymer complexes obey the thermally activated Arrhenius process which is defined by the given relation:

$$\sigma = \sigma_0 exp\left(^{-E_a}/_{KT} \right) \tag{5}$$

σ_0 represents the preexponential factor, E_a is the activation energy, and K denotes the Boltzmann constant. By linear fitting of the plot, the slope can be obtained. The activation energy (E_a) of all the polymer membranes is determined

Fig. 7 **a** Temperature-dependent conductivity plot for TSP. **b** Temperature-dependent conductivity plot for TSP with salt-doped SPEs
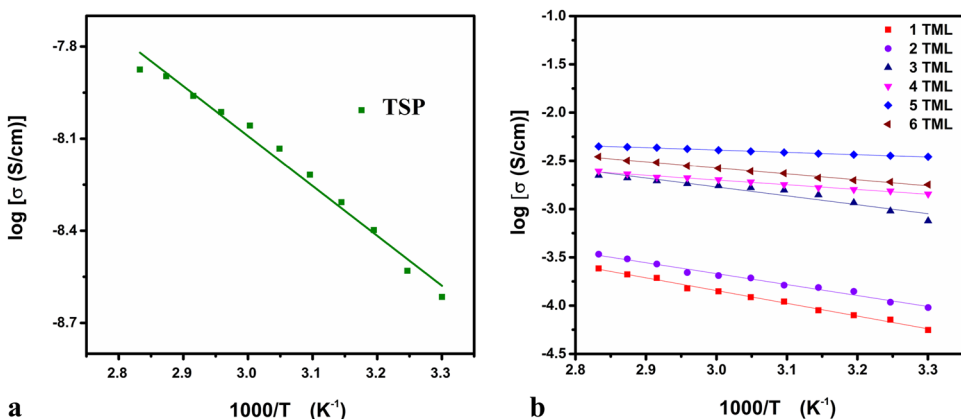
by the slope. The minimum activation energy for the optimized sample (5 TML) is 0.045 eV. The activation energy decreases as the salt concentration increases. The reason for the increased conductivity with temperature is that the vibrational modes of the polymer segments increase, and the ions move across nearby coordination sites rapidly at higher temperatures due to the greater free volume [53, 54]. As a result, hopping intrachain and interchain ion motions are encouraged, and the conductivity of the polymer electrolyte increases [55]. The values of the activation energy of all the electrolytes are given in Table 4.

Dielectric spectra

The amount of dipole alignment in a given volume is expressed by the dielectric constant (ε′). When the polarity of the electric field suddenly changes, there must be a loss of energy due to ion migration and dipole alignment which is represented by dielectric loss (ε″). These ε′ and ε″ are correlated with the conductivity of the dielectric materials [56]. Figure 8a and b represents the frequency-dependent real (ε′) and imaginary parts of the complex permittivity (ε″) of all the prepared electrolytes at room temperature. The complex permittivity can be defined by the following:

$$\varepsilon = (\varepsilon\prime - i\varepsilon'') \tag{6}$$

$$\varepsilon\prime = \left(Z'' \middle/ \omega C_0 \left(Z'^2 + Z''^2 \right) \right) \tag{7}$$

$$\varepsilon'' = \left(Z\prime \middle/ \omega C_0 \left(Z'^2 + Z''^2 \right) \right) \tag{8}$$

Here, $\varepsilon\prime$ is the dielectric constant, ε'' is the dielectric loss, ω is the angular frequency, $Z\prime$ and Z'' are the real and imaginary parts of the impedance respectively, and C_o is the vacuum capacitance [57]. Owing to the interfacial polarization, the dielectric constant ($\varepsilon\prime$) is high at low frequencies. In the polymer electrolyte, the ions tend to propagate and move along an electric field in the proper direction. With the movement of ions in the salt-added polymer matrix, the ions dissociate into anion–cation pairs. The ions are still blocked from crossing through the electrode–electrolyte contact because the electrodes do not allow charge transfer into the external circuit. At the interface between the electrode and electrolyte, these limited and reversible trapped ions subsequently gather, localize, and create a heterocharge layer. The sample is believed to be significantly thicker than this heterocharge layer which causes a sharp increase in the ε′ value. The dielectric constant rapidly decreases and becomes frequency independent in the high-frequency region. This is due to the difficulty for the charge carriers or dipoles in the polymer chain to move and orient themselves. There is virtually no extra ion diffusion in the direction of the electric field because the periodic reversal of the electric field occurs quickly [58].

The dielectric loss reaches a maximum at higher frequencies. Through internal friction, polarization produces heat and results in energy loss. Dielectric loss is a direct reflection of both the energy dissipation and the out-of-phase degree of the incident electric field [54]. The of sample 5TML has the highest values of $\varepsilon\prime$ and ε'' which is attributed to the motion of free charge carriers within the polymer matrix.
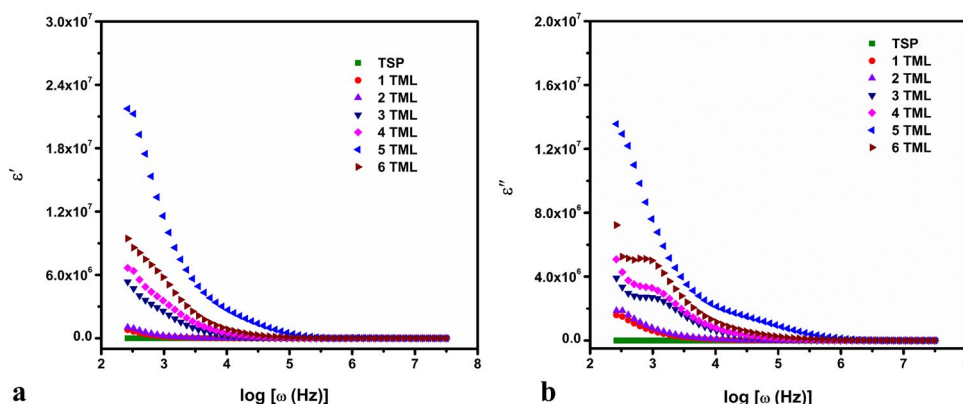
Modulus spectra

To further elucidate the dielectric behavior, modulus analysis is used. The relation between the complex permittivity and dielectric modulus is given below:

$$M\prime = \frac{\varepsilon\prime}{\varepsilon\prime^2 + \varepsilon''^2} \tag{9}$$

$$M'' = \frac{\varepsilon''}{\varepsilon\prime^2 + \varepsilon''^2} \tag{10}$$

Fig. 8 a Real part of dielectric as the function of log frequency for all the prepared electrolytes. **b** Imaginary part of dielectric as the function of log frequency for all the prepared electrolytes

Here, M^* denotes the complex dielectric modulus, and M' and M'' represent the real and imaginary parts of the dielectric modulus respectively [59]. The above formula is used for the dielectric modulus (M^*) which is inverse of the complex permittivity (ε^*). At low frequencies, the long tail is observed in M' and M'' which is due to the capacitance behavior of the electrode as shown in Fig. 9a and b. The bulk effect is the reason for the increase in the modulus with increasing frequency [60]. Both the real and imaginary parts (M' and M'') of the modulus have low values for the higher conducting sample.

Tangent analysis or dissipation factor (δ)

By investigating tan δ as a function of frequency, the dielectric relaxation parameters can be determined. The ratio of mobile to stored dipoles is expressed by the given loss tangent (δ) equation:

$$\tan\delta = \frac{\varepsilon''}{\varepsilon'} \tag{11}$$

The variation in tan δ as a function of frequency at room temperature is shown in Fig. 9 for all the prepared electrolytes. This confirms the non-Debye nature of the polymer electrolytes [61]. The frequency of the maximum tan δ value is taken for the determination of the relaxation time. The relaxation time (τ) for all the electrolytes is calculated by the following formula:

$$\tau = \frac{1}{2\pi f} = \frac{1}{\omega} \tag{12}$$

Here, τ denotes the relaxation time, and f is the maximum frequency [60]. The values of tan δ increase with salt ratio. Samples 3 TML, 4 TML, 5 TML, and 6 TML have sharp peaks. The charge carriers in the polymer chain have long-range mobility which is the reason for the increase in the relaxation frequency as well as the maximum tan δ value [62]. Figure 10 depicts the different tan δ values for the
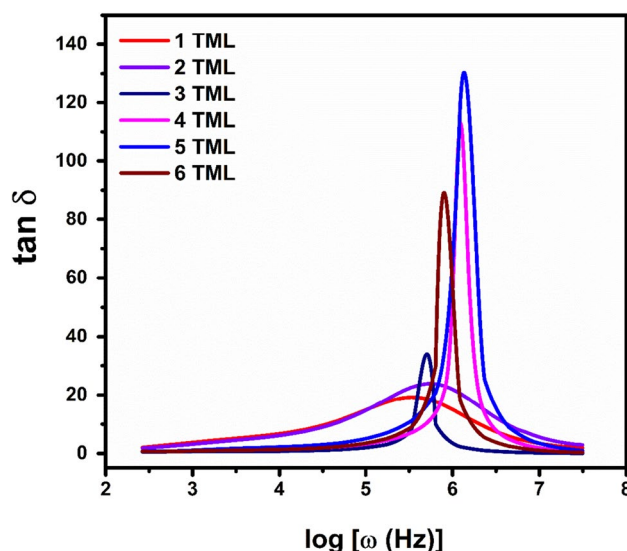
**Fig. 10** Tangent spectra of salt-added polymer electrolytes

logarithmic frequency. The relaxation time τ is determined for all the samples, and the values are given in Table 5. The lowest relaxation time is observed for sample 5 TML.

Transference number measurement

Wagner polarization method

The measurement of the transference number provides details about the role of electrons and ions in the total conductivity. The total transport number can be calculated by Wagner's polarization method. In this method, polymer electrolytes are inserted between two silver electrodes, and a fixed DC voltage of 2 V is applied. Graphite is coated on one silver electrode which acts as an electronic transport barrier. In this method, the change in the polarization current is monitored as a function of time until a steady state is reached [47, 63]. The transference number of ions (t_{ion}) and electrons (t_{ele}) is calculated by the following:

Fig. 9 **a** Real part of modulus spectra of salt added polymer electrolytes. **b** Imaginary part of modulus spectra of salt-added polymer electrolytes
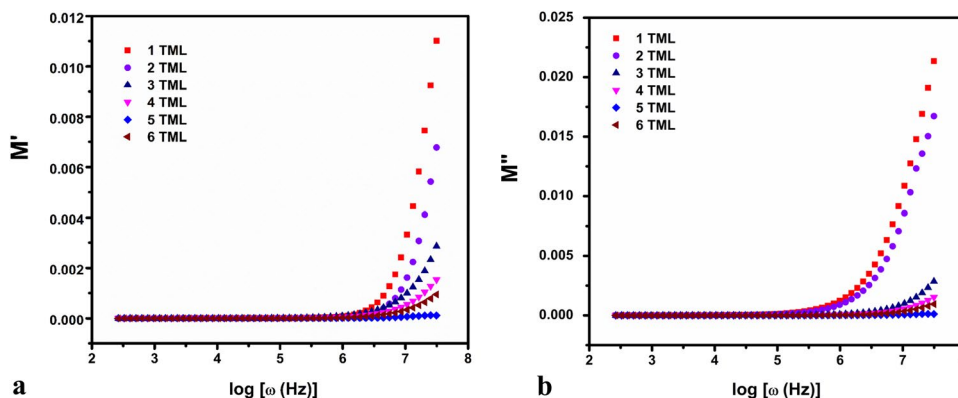
Table 5 Relaxation time and transference number of prepared polymer electrolytes

Samples	Relaxation time (τ) in s	t_{ion}	t_{ele}
1 TML	3.16×10^{-6}	0.967	0.0325
2 TML	1.94×10^{-6}	0.974	0.0259
3 TML	1.28×10^{-6}	0.988	0.0117
4 TML	8.18×10^{-7}	0.997	0.0022
5 TML	$\mathbf{7.94 \times 10^{-7}}$	**0.999**	**0.0008**
6 TML	1.25×10^{-6}	0.998	0.0010

$$t_{ion} = \left[\left(I_i - I_f \right) / I_i \right] \tag{13}$$

$$t_{ele} = \left(1 - t_{ion} \right) \tag{14}$$

Here, t_{ion} is the transport number of ions, t_{ele} is the transport number of electrons, I_i is the initial current, and I_f is the final current. When the DC voltage is applied, the initial current is detected owing to both electron and ion motion, and it rapidly decreases with time. A steady state is reached when only a small amount of constant current persists after all the ions have been drained. Under these conditions, electrons induce the final current [63]. The transport number of ions reached a maximum (0.999) for the higher conducting sample 5 TML. The values of t_{ion} and t_{ele} are given in Table 5 for all the samples. The polarization current versus time plot for the sample with the highest conductivity is displayed in Fig. 11.

Symmetrical supercapacitor device characterization

Linear sweep voltammetry (LSV)

The LSV is observed for the higher conducting sample 5 TML as shown in Fig. 12. The electrochemical stability and potential of the electrolyte are examined using linear sweep voltammetry (LSV) [64]. The LSV curve implies a slight increase in the current at the beginning. At the cutoff voltage, the current starts increasing suddenly due to the decay of the polymer electrolyte. When the potential is greater than 1.7 V, the current suddenly increases. The 5TML has a potential window of 1.7 V.
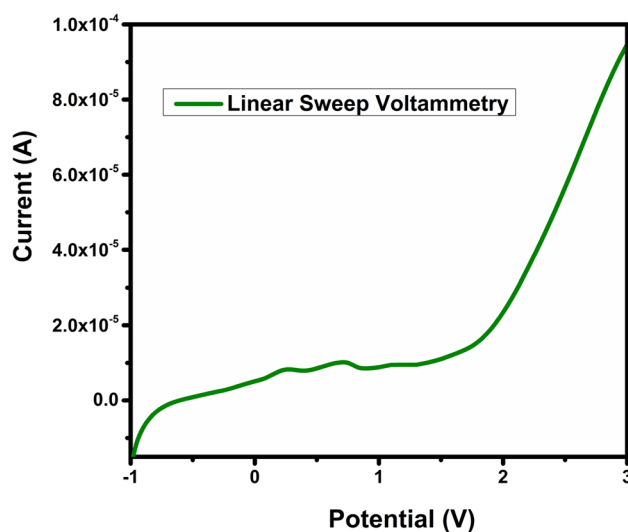
Cyclic voltammetry (CV)

The CV curves are recorded at various scan rates (15–100 mV/s) in a potential window spanning from -0.7 to 1 V and displayed in Fig. 13. The specific capacitance of the device can be calculated by the following formula:
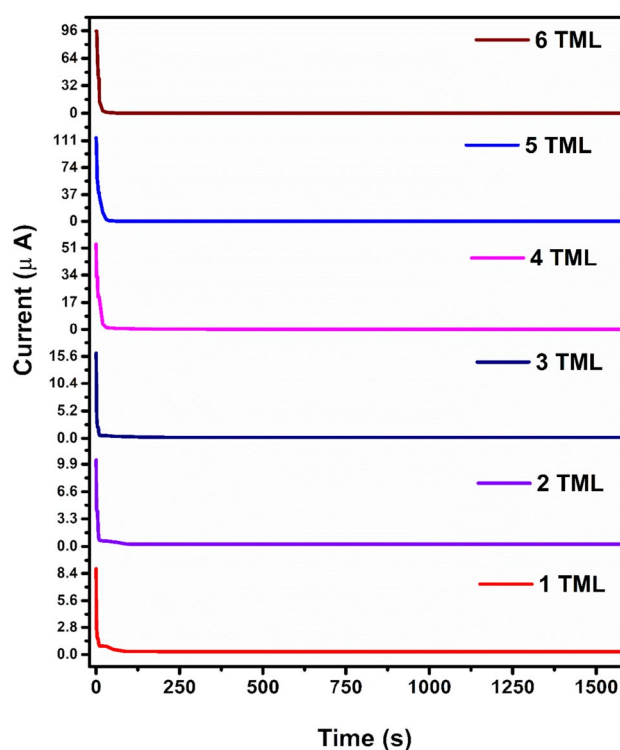
Fig. 11 Plot of polarization current vs time

$$C_{sp} = \frac{A}{m \times v \times \Delta V} \tag{15}$$

Here, A is the area of the CV curve, m is the mass of the active material, v is the scan rate, and ΔV is the potential window [65]. Figure 13 shows a CV curve with a leaf-like shape. Changes in the shape of the curve may be caused by
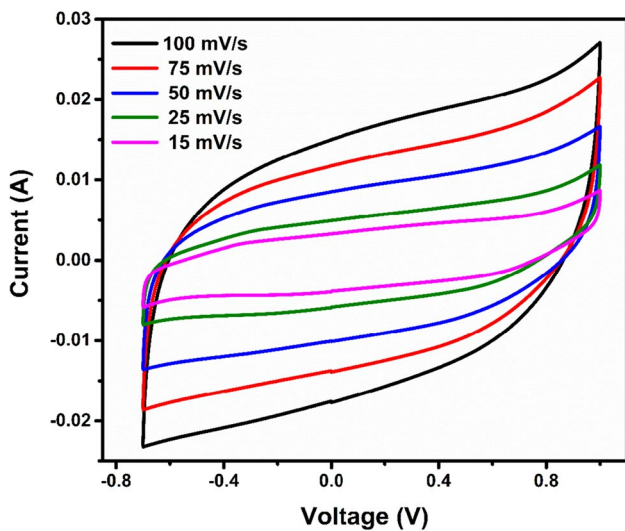

Fig. 12 Linear sweep voltammetry

Fig. 13 Cyclic voltammetry of fabricated supercapacitor device

surface, more energy is stored at lower scan rates. Consequently, this mechanism explains how potential energy is stored as a result of the double-layer charge that forms on the surfaces of carbon electrodes [67–69]. At a low scan rate of 15 mV/s, the specific capacitance is calculated to be 413.05 Fg^{-1} with a potential window of 1.7 V. The specific capacitance values for the different scan rates are given in Table 6. However, the charge and discharge processes take less time to complete, and there is insufficient contact between the electrodes and the ions at faster scan rates which decreases the amount of energy that can be stored. The performance of the fabricated supercapacitor in terms of specific capacitance is compared with the earlier reported literature and tabulated in Table 7. From this, it is confirmed that the supercapacitor performs well.

Galvanostatic charge−discharge (GCD)

For the investigations of cyclic stability and the charge−discharge process, GCD observations are used. The current density is varied from 3 to 7 mA/g to observe the charge−discharge characteristics as shown in Fig. 14. The nature of the EDLC is observed in the symmetrical charge−discharge process in the potential range of −0.7 to 1 V. By varying the applied current, the charge−discharge time is varied. When a current density of 7 mA/g is applied, the discharge time is minimal, and the charge−discharge curve is changed by varying the current density as shown in Fig. 14. The maximum discharge time is observed at a current density of 3 mA/g.

the internal resistance and porosity of the carbon electrodes at the electrode–electrolyte interface, which stimulates the formation of an electric double layer and improves the energy storage capacity of the EDLC [66]. In the anodic and cathodic areas of the EDLC, charge storage is achieved at each interface via a non-Faradaic mechanism. However, no peaks are observable in the plot, which indicates the absence of oxidation or reduction in the entire system. Since most of the ions have enough time to absorb on the electrolyte

Table 6 Value of specific capacitance, power density, and energy density

Cyclic voltammetry		Galvanostatic charge–discharge characteristics			
Scan rate (mV/s)	Specific capacitance (C_s) in F/g	Current density (A/g)	Specific capacitance (C_s) in F/g	Power density (W/kg)	Energy density (Wh/kg)
100	285.9	0.007	211.2	3499	49.8
75	302.9	0.006	213.1	2999	50.3
50	332.2	0.005	255.8	2499	60.4
25	379.4	0.004	278.3	2184	65.7
15	413.0	0.003	427.0	1499	100.8

Table 7 Specific capacitance values from literature

| SPEs	Salt	Specific capacitance (Fg^{-1})	Reference
Chitosan	Magnesium chloride	117	Hamsan, M. (2020) et al. [71]
Chitosan	Magnesium acetate	78.2	H. M. Hamsan (2020) et al. [72]
Cellulose acetate	Magnesium triflate	13.14	Gokul Gopinath (2023) et al. [73]
Chitosan/methylcellulose	Magnesium acetate	47.4	Elham M. A. Dannoun (2020) et al. [74]
Dextran/chitosan	Magnesium acetate	39.68	Ahmad S. F. M. Asnawi (2020) et al. [75]
Tamarind gum	Magnesium chloride	413.05	Present work
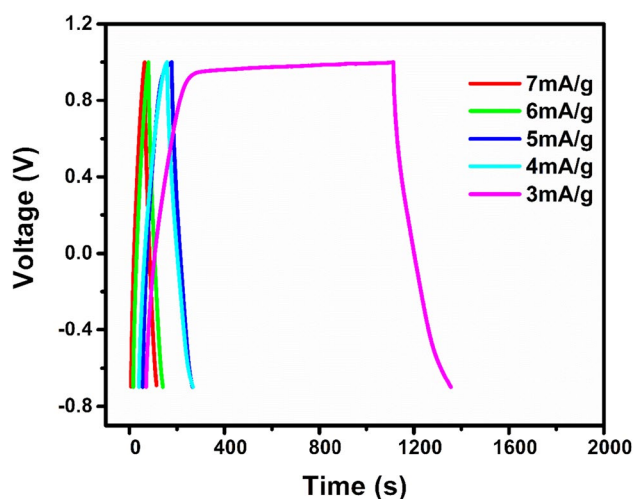
Fig. 14 GCD curves of the device with different current densities

Fig. 15 Ragone plot for the fabricated supercapacitor

At a high current density, this occurs due to the delayed movement of ions in the electrolyte to the electrode surface. Using this discharge time, the specific capacitance can be calculated. Energy density and power density values can be calculated from the GCD. [18]. From the GCD characteristics, the energy density and power density can be calculated by the following formulas:

$$E = \frac{1}{2} C_{sp} V^2 \tag{16}$$

$$P = \frac{E}{\Delta t} \tag{17}$$

Here, E represents the energy density (WhKg^{-1}), P denotes the power density (W kg^{-1}), Δt is the discharge time (s), and V is the potential window (V). When a 0.003-A current is applied, the maximum specific capacitance observed is 427 Fg^{-1}. The calculated specific capacitance, power density, and energy density values are given in Table 6.

Ragone plot

Ragone plot is plotted between energy density and power density of the device for the various current densities which are given in Fig. 15. Increasing the current density value from 3 to 7 mA, the value of power density is increased.

Figure 16 illustrates the variations in energy density (E) and power density (P) of the constructed EDLC over 1000 cycles. The stored energy starts at 3 Wh·kg^{-1} during the first cycle and eventually stabilizes at the same value. The observed power density of 1500 W/kg is stable after the 1000 cycles. This happens during the fast charge–discharge process, and the cation and anion do not reassociate to create
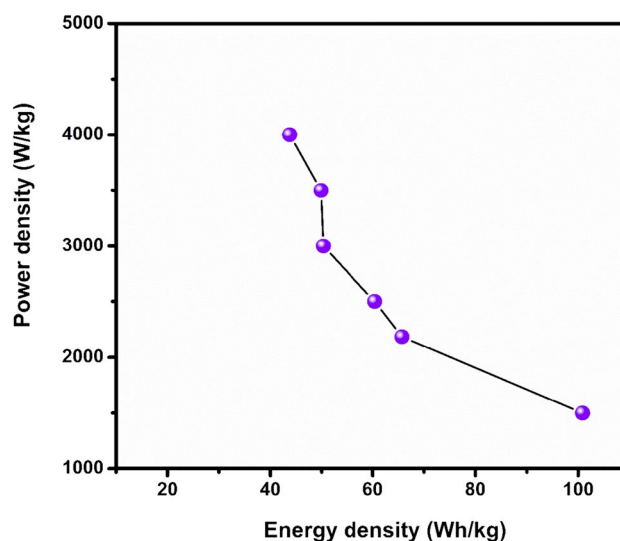
ion aggregation, which delays ionic transport. As a result, the ion adsorption at the electrode and electrolyte interface is improved [70]. Similarly, the energy density of the EDLC is also almost give the same results. The slight decrease in the energy density is noticed in the energy density values while increasing the cycles.

Conclusion

Tamarind gum-based magnesium ion-conducting polymer electrolytes are prepared by a simple solution-casting method using magnesium chloride. Structural analysis is carried out by XRD and FTIR analysis. A glass transition temperature of 127 °C is observed for sample 5 TML which
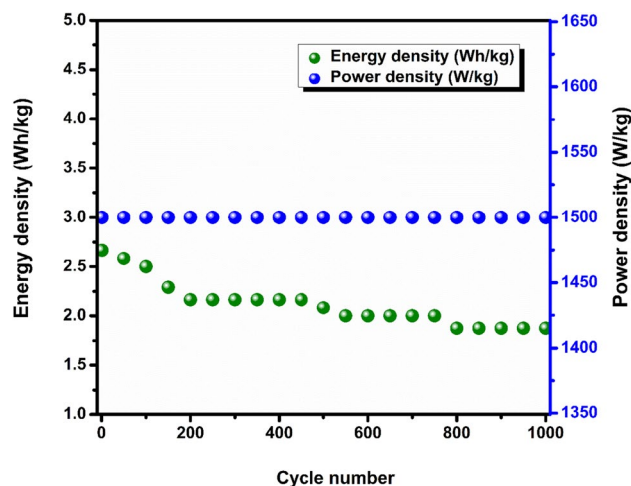

Fig. 16 Cyclic stability of the device

is due to the elongation of the polymer chain. The maximum ionic conductivity is calculated for sample 5 with a TML of 3.48×10^{-3} S/cm at ambient temperature. The conduction mechanism of the higher conducting electrolyte follows three models in which region I obeys the overlapping-large polaron tunneling (OLPT) model. The quantum mechanical tunneling model (QMT) is observed in region II, and the nonoverlapping small polaron tunneling (NSPT) model is observed in region III. The minimum activation energy of 0.045 eV is observed for sample 5 TML according to the Arrhenius plot. The tangential spectra are used for investigating the relaxation time (τ), and the higher conducting sample has the lowest relaxation time (τ) of 7.94×10^{-7} s. The movement of magnesium ions in the polymer electrolyte is responsible for this maximum ionic conductivity, which is confirmed by Wagner's DC polarization method. The supercapacitor shows EDLC behavior with a specific capacitance of 413.05 Fg^{-1} at a scan rate of 15 mV/s as determined by cyclic voltammetry (CV). From the GCD analysis, the power and energy density are calculated as 1499 W/kg and 100 Wh/kg, respectively. The performance of the supercapacitor is compared with the earlier reports and presents better specific capacitance. The cyclic stability of the device is confirmed by the observed values of power and energy density for different cycles up to 1000. Therefore, it is concluded that the prepared electrolyte is a worthy candidate for energy storage applications.

Data availability No datasets were generated or analysed during the current study.

Declarations

Conflict of interest The authors declare no competing interests.

References

1. Aziz SB, Nofal MM, Abdulwahid RT, Ghareeb HO, Dannoun EMA, Abdullah RM, Hamsan MH, Kadir MFZ (2021) Plasticized sodium-ion conducting PVA based polymer electrolyte for electrochemical energy storage—EEC modeling, transport properties, and charge-discharge characteristics. Polymers (Basel) 13:803

2. Siwal SS, Zhang Q, Devi N, Thakur VK (2020) Carbon-based polymer nanocomposite for high-performance energy storage applications. Polymers (Basel) 12:1–31

3. Vanitha D, Asath S, Nallaperumal B, Bahadur SA, Nallamuthu N, Athimoolam S, Manikandan A (2016) Electrical impedance studies on sodium ion conducting composite blend polymer electrolyte. J Inorg Organomet Polym Mater 27:257–65

4. Kumar KN, Sreekanth T, Reddy MJ, Rao UVS (2001) Study of transport and electrochemical cell characteristics of PVP: NaClO 3 polymer electrolyte system. J Power Sources 101:130–133

5. Samsudin AS, Saadiah MA (2018) Ionic conduction study of enhanced amorphous solid bio-polymer electrolytes based carboxymethyl cellulose doped NH4Br. J Non Cryst Solids 497:19–29

6. Selvalakshmi S, Vanitha D, Saranya P, Selvalsekarapandian S, Mathavan T, Premalatha M (2022) Structural and conductivity studies of ammonium chloride doped agar-agar biopolymer electrolytes for electrochemical devices. J Mater Sci Mater Electron 33:24884–24894

7. Lima E, Raphael E, Sentanin F, Rodrigues LC, Ferreira RAS, Carlos LD, Silva MM, Pawlicka A (2012) Photoluminescent polymer electrolyte based on agar and containing europium picrate for electrochemical devices. Mater Sci Eng B Solid State Mater Adv Technol 177:488–493

8. Hou X, Xue Z, Liu J, Yan M, Xia Y, Ma Z (2019) Characterization and property investigation of novel eco-friendly agar/carrageenan/TiO2 nanocomposite films. J Appl Polym Sci 136:1–12

9. Idris NH, Senin HB, Arof AK (2007) Dielectric spectra of LiTFSI-doped chitosan/PEO blends. Ionics (Kiel) 13:213–217

10. Maheshwari T, Tamilarasan K, Selvasekarapandian S, Chitra R, Muthukrishnan M (2022) Synthesis and characterization of dextran, poly (vinyl alcohol) blend biopolymer electrolytes with NH4NO3, for electrochemical applications. Int J Green Energy 19:314–330

11. Aziz SB, Dannoun EMA, Abdalrahman AA, Abdulwahid RT, Al-Saeedi SI, Brza MA, Nofal MM, Abdullah RM, Hadi JM, Karim WO (2022) Characteristics of methyl cellulose based solid polymer electrolyte inserted with potassium thiocyanate as K+ cation provider: structural and electrical studies. Materials 15:5579

12. Shuhaimi NEA, Alias NA, Kufian MZ, Majid SR, Arof AK (2010) Characteristics of methyl cellulose-NH 4NO 3-PEG electrolyte and application in fuel cells. J Solid State Electrochem 14:2153–2159

13. Shuhaimi NEA, Majid SR, Arof AK (2009) On complexation between methyl cellulose and ammonium nitrate. Mater Res Innovations 13:239–242

14. Nandhinilakshmi M, Vanitha D, Nallamuthu N, Sundaramahalingam K, Saranya P (2022) Dielectric relaxation behaviour and ionic conductivity for corn starch and PVP with sodium fluoride. J Mater Sci Mater Electron 33:12648–12662

15. Muthukrishnan M, Shanthi C, Selvasekarapandian S, Manjuladevi R, Perumal P, Chrishtopher Selvin P (2019) Synthesis and characterization of pectin-based biopolymer electrolyte for electrochemical applications. Ionics (Kiel) 25:203–214

16. Moniha V, Alagar M, Selvasekarapandian S, Sundaresan B, Boopathi G (2018) Conductive bio-polymer electrolyte iota-carrageenan with ammonium nitrate for application in electrochemical devices. J Non Cryst Solids 481:424–434

17. Nandhinilakshmi M, Vanitha D, Nallamuthu N, Sundaramahalingam K, Saranya P (2022) Investigation on conductivity and optical properties for blend electrolytes based on iota-carrageenan and acacia gum with ethylene glycol. J Mater Sci Mater Electron 33:21172–21188

18. Nandhinilakshmi M, Vanitha D, Nallamuthu N, Sundaramahalingam K, Saranya P (2023) Fabrication of symmetric super capacitor using lithium - ion conducting IOTA carrageenan - based

biopolymer electrolytes. J Polym Environ. https://doi.org/10.1007/s10924-023-03014-6

19. Saranya P, Vanitha D, Sundaramahalingam K, Nandhinilakshmi M (2023) A study of optical properties of coppersulphate pentahydrate doped IOTA-carrageenan polymer electrolytes. J Elastomers Plast 55(6):884–895. https://doi.org/10.1177/00952443231184608

20. Gnana Kiran M, Krishna Jyothi N, Samatha K, Rao MP, Vijayakumar K (2020) Optical properties of TSP: NaNO3 biopolymer electrolyte. Res J Chem Environ 24:27–35

21. Saranya P, Vanitha D, Sundaramahalingam K, Nandhinilakshmi M, Samad SA (2023) Structural and electrical properties of cross-linked blends of xanthan gum and polyvinylpyrrolidone - based solid polymer electrolyte. Ionics (Kiel) 29(12):5147–59. https://doi.org/10.1007/s11581-023-05219-0

22. Premalatha M, Mathavan T, Selvasekarapandian S, Selvalakshmi S (2018) Structural and electrical characterization of tamarind seed polysaccharide (TSP) doped with NH4HCO2. AIP Conf Proc 070005:4–8

23. Kumar LS, Selvin PC, Selvasekarapandian S, Manjuladevi R, Monisha S (2018) Tamarind seed polysaccharide biopolymer membrane for lithium-ion conducting battery. Ionics (Kiel) 24:3793–3803

24. Premalatha M, Mathavan T, Selvasekarapandian S, Monisha S (2017) Tamarind seed polysaccharide (TSP)-based Li-ion conducting membranes. Ionics (Kiel) 23:2677–2684. https://doi.org/10.1007/s11581-017-1989-x

25. Koliyoor J, Ismayil, Hegde S, Sanjeev G, Murari MS (2023) An insight into the suitability of magnesium ion-conducting biodegradable methyl cellulose solid polymer electrolyte film in energy storage devices. J Mater Sci. 58:5389–5412

26. Ngai KS, Ramesh S, Ramesh K, Juan JC (2016) A review of polymer electrolytes: fundamental, approaches and applications. Ionics (Kiel) 22:1259–1279

27. Yassin AY (2020) Dielectric spectroscopy characterization of relaxation in composite based on (PVA–PVP) blend for nickel–cadmium batteries. J Mater Sci Mater Electron 31:19447–19463

28. Khanmirzaei MH, Ramesh S, Ramesh K (2015) Effect of different iodide salts on ionic conductivity and structural and thermal behavior of rice-starch-based polymer electrolytes for dye-sensitized solar cell application. Ionics (Kiel). https://doi.org/10.1007/s11581-015-1385-3

29. Malaysiana S, Diperbadankan CI, Berasaskan PE, Elektrik S (2014) Ionic liquid incorporated PVC based polymer electrolytes : electrical and dielectric properties. Sains Malays 43:877–883

30. Pasini Cabello SD, Ochoa NA, Takara EA, Mollá S, Compañ V (2017) Influence of pectin as a green polymer electrolyte on the transport properties of chitosan-pectin membranes. Carbohydr Polym 157:1759–1768

31. Kumar KK, Ravi M, Pavani Y, Bhavani S, Sharma AK, Narasimha Rao VVR (2012) Electrical conduction mechanism in NaCl complexed PEO/PVP polymer blend electrolytes. J Non Cryst Solids 358:3205–3211

32. Di Noto V, Münchow V, Vittadello M, Collet JC, Lavina S (2002) Synthesis, characterization and conductivity studies of Li and Mg polymer electrolytes based on esters of ethylenediaminetetraacetic acid and PEG400. Solid State Ion 147:397–402

33. Sengwa RJ, Dhatarwal P, Choudhary S (2014) Role of preparation methods on the structural and dielectric properties of plasticized polymer blend electrolytes: correlation between ionic conductivity and dielectric parameters. Electrochim Acta 142:359–370

34. Basha SKS, Rao MC (2018) Spectroscopic and electrochemical properties of PVP based polymer electrolyte films. Polym Bull 75:3641–3666

35. Sundar M, Selladurai S (2006) Effect of fillers on magnesium-poly(ethylene oxide) solid polymer electrolyte. Ionics (Kiel) 12:281–286

36. Ponraj T, Ramalingam A, Selvasekarapandian S, Srikumar SR, Manjuladevi R (2021) Plasticized solid polymer electrolyte based on triblock copolymer poly(vinylidene chloride-co-acrylonitrile-co-methyl methacrylate) for magnesium ion batteries. Polym Bull 78:35–57

37. Sampathkumar L, Selvin PC, Selvasekarapandian S, Perumal P, Chitra R, Muthukrishnan M (2019) Synthesis and characterization of biopolymer electrolyte based on tamarind seed polysaccharide, lithium perchlorate and ethylene carbonate for electrochemical applications. Ionics (Kiel) 25:1067–1082

38. Anilkumar KM, Jinisha B, Manoj M, Jayalekshmi S (2017) Poly(ethylene oxide) (PEO) – poly(vinyl pyrrolidone) (PVP) blend polymer based solid electrolyte membranes for developing solid state magnesium ion cells. Eur Polym J 89:249–262

39. Ahmed MB, Nofal MM, Aziz SB, Al-Saeedi SI, Brza MA, Dannoun EMA, Murad AR (2022) The study of ion transport parameters associated with dissociated cation using EIS model in solid polymer electrolytes (SPEs) based on PVA host polymer: XRD, FTIR, and dielectric properties. Arab J Chem 15:104196

40. Kumar LS, Selvasekarapandian PCSS (2020) Impact of lithium triflate (LiCF3SO3) salt on tamarind seed polysaccharide-based natural solid polymer electrolyte forfor application in electrochemical device. Polym Bull. https://doi.org/10.1007/s00289-020-03185-5

41. Yang Y, Huo H (2013) Investigation of structures of PEO-MgCl2 based solid polymer electrolytes. J Polym Sci B Polym Phys 51:1162–1174

42. Premalatha M, Mathavan T, Selvasekarapandian S, Monisha S, Pandi DV, Selvalakshmi S (2016) Investigations on proton conducting biopolymer membranes based on tamarind seed polysaccharide incorporated with ammonium thiocyanate. J Non Cryst Solids 453:131–140

43. He R, Kyu T (2016) Effect of plasticization on ionic conductivity enhancement in relation to glass transition temperature of crosslinked polymer electrolyte membranes. Macromolecules 49:5637–5648

44. Shanmuga Priya S, Karthika M, Selvasekarapandian S, Manjuladevi R (2018) Preparation and characterization of polymer electrolyte based on biopolymer I-carrageenan with magnesium nitrate. Solid State Ion 327:136–149

45. Noor NAM, Isa MIN (2019) Investigation on transport and thermal studies of solid polymer electrolyte based on carboxymethyl cellulose doped ammonium thiocyanate for potential application in electrochemical devices. Int J Hydrogen Energy 44:8298–8306

46. Ramaswamy M, Malayandi T, Subramanian S, Srinivasalu J, Rangaswamy M (2017) Magnesium ion conducting polyvinyl alcohol–polyvinyl pyrrolidone-based blend polymer electrolyte. Ionics (Kiel) 23:1771–1781

47. Kiruthika S, Malathi M, Selvasekarapandian S, Tamilarasan K, Moniha V, Manjuladevi R (2019) Eco-friendly biopolymer electrolyte, pectin with magnesium nitrate salt, for application in electrochemical devices. J Solid State Electrochem 23:2181–2193

48. Kiruthika S, Malathi M, Selvasekarapandian S, Tamilarasan K, Maheshwari T (2020) Conducting biopolymer electrolyte based on pectin with magnesium chloride salt for magnesium battery application. Polym Bull 77:6299–6317

49. Jothi MA, Vanitha D, Bahadur SA, Nallamuthu N (2021) Promising biodegradable polymer blend electrolytes based on cornstarch : PVP for electrochemical cell applications. Bull Mater Sci 0123456789:1–12

50. Hafiza MN, Isa MIN (2014) Ionic conductivity and conduction mechanism studies of CMC/ chitosan biopolymer blend electrolytes. Res J Recent Sci 3:50–56

51. Sohaimy MIH, Isa MIN (2016) Ionic conductivity and conduction mechanism studies on cellulose based solid polymer electrolytes doped with ammonium carbonate. Polym Bull 74:1371–1386. https://doi.org/10.1007/s00289-016-1781-5

52. Jothi MA, Vanitha D, Bahadur SA, Nallamuthu N (2021) Proton conducting polymer electrolyte based on cornstarch, PVP, and NH4Br for energy storage applications. Ionics (Kiel) 27:225–237

53. Kingslin Mary Genova F, Selvasekarapandian S, Vijaya N, Sivadevi S, Premalatha M, Karthikeyan S (2017) Lithium ion-conducting polymer electrolytes based on PVA–PAN doped with lithium triflate. Ionics (Kiel) 23:2727–2734

54. Manjuladevi R, Thamilselvan M, Selvasekarapandian S, Christopher Selvin P, Mangalam R, Monisha S (2018) Preparation and characterization of blend polymer electrolyte film based on poly(vinyl alcohol)-poly(acrylonitrile)/MgCl2 for energy storage devices. Ionics (Kiel) 24:1083–1095

55. Baskaran R, Selvasekarapandian S, Kuwata N, Kawamura J, Hattori T (2006) Conductivity and thermal studies of blend polymer electrolytes based on PVAc-PMMA. Solid State Ion 177:2679–2682

56. Verma ML, Sahu HD (2017) Study on ionic conductivity and dielectric properties of PEO-based solid nanocomposite polymer electrolytes. Ionics (Kiel). https://doi.org/10.1007/s11581-017-2063-4

57. Premalatha M, Vijaya N, Selvasekarapandian S, Selvalakshmi S (2016) Characterization of blend polymer PVA-PVP complexed with ammonium thiocyanate. Ionics (Kiel) 22:1299–1310

58. Woo HJ, Majid SR, Arof AK (2012) Dielectric properties and morphology of polymer electrolyte based on poly(ε-caprolactone) and ammonium thiocyanate. Mater Chem Phys 134:755–761

59. Hadi JM, Aziz SB, Mustafa MS, Hamsan MH, Abdulwahid RT, Kadir MFZ, Ghareeb HO (2020) Role of nano-capacitor on dielectric constant enhancement in PEO:NH4SCN:xCeO2 polymer nano-composites: electrical and electrochemical properties. J Market Res 9:9283–9294

60. Nandhinilakshmi M, Vanitha D, Nallamuthu N, Anandha Jothi M, Sundaramahalingam K (2022) Structural, electrical behavior of sodium ion-conducting corn starch–PVP-based solid polymer electrolytes. Polym Bull. https://doi.org/10.1007/s00289-022-04230-1

61. Mohamad AH, Abdullah OG, Saeed SR (2020) Effect of very fine nanoparticle and temperature on the electric and dielectric properties of MC-PbS polymer nanocomposite films. Results Phys 16:102898

62. Ahmed HT, Abdullah OG (2020) Impedance and ionic transport properties of proton-conducting electrolytes based on polyethylene oxide/methylcellulose blend polymers. J Sci Adv Mater Dev 5:125–133

63. Chitra R, Sathya P, Selvasekarapandian S, Meyvel S (2020) Synthesis and characterization of iota-carrageenan biopolymer electrolyte with lithium perchlorate and succinonitrile (plasticizer). Polym Bull 77:1555–1579

64. Yusof YM, Shukur MF, Hamsan MH, Jumbri K, Kadir MFZ (2019) Plasticized solid polymer electrolyte based on natural polymer blend incorporated with lithium perchlorate for electrical double-layer capacitor fabrication. Ionics (Kiel) 25:5473–5484

65. Hadi JM, Aziz SB, Saeed SR, Brza MA, Abdulwahid RT, Hamsan MH, Abdullah RM, Kadir MFZ, Muzakir SK (2020) Investigation of ion transport parameters and electrochemical performance of plasticized biocompatible chitosan-based proton conducting polymer composite electrolytes. Membranes (Basel) 10:1–27

66. Francis KA, Liew CW, Ramesh S, Ramesh K, Ramesh S (2016) Ionic liquid enhanced magnesium-based polymer electrolytes for electrical double-layer capacitors. Ionics (Kiel) 22:919–925

67. Nadiah NS, Omar FS, Numan A, Mahipal YK, Ramesh S, Ramesh K (2017) Influence of acrylic acid on ethylene carbonate/dimethyl carbonate based liquid electrolyte and its supercapacitor application. Int J Hydrogen Energy 42:30683–30690

68. Aziz SB, Asnawi ASFM, Mohammed PA, Abdulwahid RT, Yusof YM, Abdullah RM, Kadir MFZ (2021) Impedance, circuit simulation, transport properties and energy storage behavior of plasticized lithium ion conducting chitosan based polymer electrolytes. Polym Test 101:107286

69. Wang J, Zhao Z, Muchakayala R, Song S (2018) High-performance Mg-ion conducting poly(vinyl alcohol) membranes: preparation, characterization and application in supercapacitors. J Memb Sci 555:280–289

70. Nandhinilakshmi M, Vanitha D, Nallamuthu N, Sundaramahalingam K, Saranya P, Shameem A (2023) Fabrication of high-performance symmetrical supercapacitor using lithium iodide-based biopolymer electrolyte. Ionics (Kiel). https://doi.org/10.1007/s11581-023-05270-x

71. Hamsan MH, Aziz SB, Nofal MM, Brza MA, Abdulwahid RT, Hadi JM, Karim WO, Kadir MFZ (2020) Characteristics of EDLC device fabricated from plasticized chitosan:MgCl2 based polymer electrolyte. J Mater Res Technol 9:10635–10646

72. Hamsan MH, Aziz SB, Kadir MFZ, Brza MA, Karim WO (2020) The study of EDLC device fabricated from plasticized magnesium ion conducting chitosan based polymer electrolyte. Polym Test 90:106714

73. Gopinath G, Shanmugaraj P, Sasikumar M, Shadap M, Banu A, Ayyasamy S (2023) Cellulose acetate-based magnesium ion conducting plasticized polymer membranes for EDLC application: advancement in biopolymer energy storage devices. Appl Surf Sci Adv 18:100498

74. Dannoun EMA, Aziz SB, Brza MA, Nofal M, Hamsan MH, Kadir MFZ, Woo HJ (2020) The study of plasticized solid polymer blend electrolytes based on natural polymers and their application for energy storage EDLC devices. Polymers (Basel) 12:2531

75. Asnawi ASFM, Aziz SB, Saeed SR, Yusof YM, Abdulwahid RT, Al-Zangana S, Karim WO, Kadir MFZ (2020) Solid-state edlc device based on magnesium ion-conducting biopolymer composite membrane electrolytes: impedance, circuit modeling, dielectric properties and electrochemical characteristics. Membranes (Basel) 10:1–20